



# **Low-level atmospheric turbulence dataset in China generated by combining radar wind profiler and radiosonde observations**

Deli Meng<sup>a, b</sup>, Jianping Guo<sup>a, d\*</sup>, Juan Chen<sup>c</sup>, Xiaoran Guo<sup>a</sup>, Ning Li<sup>a</sup>, Yuping  
Sun<sup>a</sup>, Zhen Zhang<sup>a, c</sup>, Na Tang<sup>a</sup>, Hui Xu<sup>a</sup>, Tianmeng Chen<sup>a</sup>, Rongfang Yang<sup>f</sup>,  
Jiajia Hua<sup>b</sup>

<sup>a</sup>State Key Laboratory of Severe Weather Meteorological Science and  
Technology, Chinese Academy of Meteorological Sciences, Beijing 100081, China

<sup>b</sup>Xiong'an Atmospheric Boundary Layer Key Laboratory of China  
Meteorological Administration, Beijing 100085, China

<sup>c</sup>AVIC Leihua Electronic Technology Research Institute, Wuxi 214063, China

<sup>d</sup>Guizhou New Meteorological Technology Co., Ltd, Guiyang 550001, China

<sup>e</sup>Department of Atmospheric and Oceanic Sciences & Institute of Atmospheric  
Sciences, Fudan University, Shanghai 200438, China

<sup>f</sup>Hebei Meteorological Technology and Equipment Center, Shijiazhuang 050022,  
China

*\*Correspondence to:* Dr/ Prof. Jianping Guo (Email: [jpguocams@gmail.com](mailto:jpguocams@gmail.com))



## Abstract

Low-level atmospheric turbulence plays a critical role in cloud dynamics and aviation safety. Nevertheless, height-resolved turbulence profiles remain scarce, largely owing to observational challenges. By leveraging collocated radar wind profiler (RWP) and radiosonde observations from 29 stations across China during 2023, a high-resolution dataset of low-level turbulence-related parameters are generated based on spectral width method. This dataset includes squared Brunt–Vaisala frequency ( $N^2$ ), turbulent dissipation rate ( $\varepsilon$ ), vertical eddy diffusivity ( $K$ ), inner scale ( $l_0$ ), and buoyancy length scale ( $L_B$ ), which are provided twice daily at 00 and 12 UTC with a vertical resolution of 120 m, covering altitudes from 0.12 km to 3.0 km above ground level. Spatial analysis reveals significant regional disparities in turbulence-related parameters across China, where  $\varepsilon$ ,  $K$  and  $L_B$  are higher in northwest and north China compared to south China, while  $N^2$  and  $l_0$  display an inverse spatial pattern. This contrasting geographical distributions suggest distinct atmospheric instability across China. In terms of seasonality, turbulence-related variables showed maxima during spring and summer. Vertical profiles characteristics show distinct altitudinal dependencies,  $\varepsilon$ ,  $L_B$  and  $K$  exhibit progressive attenuation with altitude, while  $N^2$  and  $l_0$  increase with height. Statistical analysis indicates that  $\varepsilon$  and  $K$  follow log-normal distributions, whereas  $l_0$  and  $L_B$  align with Gamma distributions. This dataset is publicly accessible <https://doi.org/10.5281/zenodo.14959025> (Meng and Guo, 2025), which provides crucial insights into the fine-scale structural evolution of low-level turbulence. The preliminary findings based on the dataset have great implications for improving our understanding of pre-storm environment and conducting scientific planning and guiding of low-level flight routes in the emerging low-altitude economy in China.



55

### Short Summary

56 This study provides a high-resolution dataset of low-level atmospheric turbulence  
57 across China, using radar and weather balloon observations. It reveals regional and  
58 seasonal variations in turbulence, with stronger activity in spring and summer. The  
59 dataset supports weather forecasting, aviation safety, and low-altitude flight planning,  
60 aiding China's growing low-altitude economy and accessible  
61 at <https://doi.org/10.5281/zenodo.14959025>.

62

63



64

## 65 **1 Introduction**

66 The low-level atmosphere below 3 km altitude serves as a critical interface for  
 67 planetary boundary layer (PBL) and cloud interactions, and convective initiation  
 68 processes (Marquis et al., 2021; Nowak et al., 2021). This dynamic transition zone  
 69 facilitates exchange of water vapor, thermal energy, moment flux, and aerosol particles  
 70 between Earth's surface and free atmosphere (Muñoz-Esparza et al., 2018; Brunke et  
 71 al., 2022). The turbulence-driven exchanges can be quantitatively characterized by key  
 72 physical parameters: turbulent dissipation rate ( $\epsilon$ ), inner scale ( $l_0$ ), buoyancy length  
 73 scale ( $L_B$ ), vertical eddy diffusivity ( $K$ ), and atmospheric refractive index structure  
 74 constant ( $Cn^2$ ) (Fukao et al., 1994; Wilson, 2004). These parameters collectively  
 75 govern the energy cascade processes and momentum transfer mechanisms that  
 76 dominate PBL thermodynamics. Accurately understanding the spatiotemporal  
 77 evolution of low-level turbulence is crucial not only for improving predictive skill of  
 78 severe convective systems through refined parameterization schemes but also  
 79 implementing operational safeguards for low-altitude aviation safety.

80 Therefore, advances have been made in recent years in observational techniques  
 81 for characterizing low-level turbulence. Conventional in-situ platforms include weather  
 82 balloons (e.g., Clayson and Kantha, 2008; Kohma et al., 2019; Guo et al., 2016), rocket  
 83 (Namboodiri et al., 2011) and aircraft (Nicholls et al., 1984; Brunke et al., 2022;  
 84 Chechin et al., 2023). Concurrently, unmanned aerial vehicles (UAVs) have  
 85 demonstrated growing potential in capturing low-level turbulence features that  
 86 traditional aircraft and radiosonde networks cannot systematically resolve (Shelekhov  
 87 et al., 2021). Nevertheless, these approaches face inherent limitations, such as high  
 88 operational costs, discontinuous temporal sampling, and spatially constrained coverage  
 89 limited to point measurements or linear transects. Such restrictions fundamentally  
 90 impede the acquisition of vertically resolved turbulence profiles with sufficient  
 91 spatiotemporal continuity.





92 To address these observational gaps, ground-based lidars and radars have emerged  
 93 as pivotal solutions (Gage and Balsley, 1978). Radar wind profiler (RWP) and coherent  
 94 Doppler wind lidar systems have demonstrated effectiveness in obtaining turbulence  
 95 parameters with both high temporal resolution and operational continuity (Sato and  
 96 Woodman, 1982; Hocking, 1985; Fukao et al., 1994; Nastrom and Eaton, 1997; Luce  
 97 et al., 2023a; Meng et al., 2024).

98 Turbulence dissipation rate ( $\varepsilon$ ), in conjunction with  $l_0$ ,  $L_B$ , and  $K$  derivable from  
 99  $\varepsilon$  (Fukao et al., 1994), serve as critical determinants in radar-derived quantification of  
 100 atmospheric turbulence metrics. Three principal methodological frameworks have  
 101 emerged for retrieving  $\varepsilon$  in low-level atmosphere from RWP observations, namely the  
 102 power method (Hocking, 1985; Hocking and Mu, 1997), variance method (Satheesan  
 103 and Murthy, 2002), and Doppler spectral width method (Nastrom, 1997; Dehghan and  
 104 Hocking, 2011). The power method utilizes backscattered signal intensity modulated  
 105 by refractive index fluctuations (Weinstock, 1981a; Cohn, 1995). The variance method  
 106 establishes a direct mathematical relationship between  $\varepsilon$  and the variance of vertical  
 107 velocity (Satheesan and Murthy, 2002). Comprehensive reviews by Cohn (1995), Gage  
 108 and Balsley (1978), and Wilson (2004) have thoroughly evaluated their underlying  
 109 assumptions, advantages, and limitations. As highlighted by Satheesan and Murthy  
 110 (2002), the power method necessitates thermodynamic profiles, the variance method  
 111 demands accuracy in Doppler measurements, particularly challenged by contamination  
 112 from non-turbulent motions in vertical beam observations, while the influence of  
 113 ground clutter and the differences in the calculation of various spectral broadening  
 114 terms are the main factors contributing to the large uncertainty in turbulence spectral  
 115 width. Most widely adopted is the Doppler spectrum width technique, which isolates  
 116 turbulence-induced spectral broadening through systematic removal of non-turbulent  
 117 contributions (e.g., Cohn, 1995; Nastrom and Eaton, 1997; Eaton and Nastrom, 1998;  
 118 Jacoby-Kaoly et al., 2002; Dehghan and Hocking, 2011; Kohma et al., 2019; Jaiswal et  
 119 al., 2020; Solanki et al., 2022; Chen et al., 2022a,b; Luce et al., 2023b). The non-  
 120 turbulent spectral widths are mainly contributed by beam broadening, shear effects, and



121 gravity wave perturbations, which can be estimated by the algorithms proposed by  
 122 Hocking (1985), Nastrom (1997), and Dehghan and Hocking (2011), respectively.  
 123 Recent work (see Chen et al., 2022b) demonstrates critical vertical wind shear (VWS)  
 124 thresholds exceeding  $0.006 \text{ s}^{-1}$ , where turbulence spectral width retrievals become  
 125 increasingly susceptible to negative value artifacts, highlighting unresolved challenges  
 126 under extreme shear conditions that frequently accompany severe convective systems.

127 Complementing radar-based methodologies, the radiosonde measurements have  
 128 been long used to derive the profiles of  $\varepsilon$  using the Thorpe analysis method (Thorpe,  
 129 1977). Originally designed to diagnose turbulent overturning in the troposphere and  
 130 lower stratosphere, this method enables cross-validation with radar-derived turbulence  
 131 metrics through coordinated multi-platform campaigns (Clayson and Kantha, 2008;  
 132 Wilson et al., 2014; Li et al., 2016; Kohma et al., 2019; Jaiswal et al., 2020; Lv et al.,  
 133 2021; Rajput et al., 2022; Ko et al., 2024). Nevertheless, Thorpe analysis method is not  
 134 suitable for the turbulence retrieval in the low-level atmosphere below 3 km.

135 Even though significant stride has been made in calculating temporally  
 136 continuous profiles of  $\varepsilon$ , other turbulence-related parameters such as  $l_0$ ,  $L_B$ , and  $K$  in  
 137 the low atmosphere remains insufficiently analyzed, particularly on a national scale,  
 138 largely due to the lack of concurrent observations of high-resolution temperature,  
 139 humidity and wind profiles. Fortunately, the RWP observational network has been built  
 140 up and operated by China Meteorological Administration (CMA), and most of RWP  
 141 sites are collocated with radiosonde sites. Furthermore, attempts were made to retrieve  
 142 all the above-mentioned turbulence metrics by combining the measurements of RWP  
 143 and radiosonde by Solanki et al. (2022). This motivates us to construct such low-level  
 144 turbulence dataset in China, enabling a holistic view of the turbulence features  
 145 throughout China. The paper is structured as follows. Section 2 details the data sources  
 146 and methodology, including instrumentation specifications from the observational  
 147 station and the retrieval method employed for turbulence-related parameter. Section 3  
 148 presents a multi-scale analysis of turbulence dynamics, encompassing vertical profile  
 149 examinations and spatiotemporal variation patterns of low-level turbulence in China.



150 Finally, summary and concluding remarks are given in Section 4.

## 151 **2 Data and Methodology**

### 152 **2.1 RWP and radiosonde measurements**

153 As of December 31, 2023, CMA operates a modern vertical meteorological  
 154 observing network consisting of 120 L-band radiosonde and over 200 RWP stations.  
 155 This study Through a rigorous station selection process, 29 optimally co-located  
 156 observation stations were identified (Fig. 1) based on systematic evaluation of spatial  
 157 representativeness and instrument performance metrics. These stations are equipped  
 158 with an advanced RWP-radiosonde synergetic observation system specifically designed  
 159 for retrieving low-level turbulence-related parameters. The network spans latitudes  
 160 from 16.83°N to 49.22°N and longitudes from 75.98°E to 129.47°E, covering China's  
 161 primary geomorphological regions, ranging from coastal plains (-0.4 m above mean sea  
 162 level, AMSL) to high-mountain plateaus (4,326.8 m AMSL). Detailed station  
 163 information is provided in Table 1.

164 The RWP system provides continuous wind profiling from 0.12 km to 5.0 km  
 165 above ground level (AGL), with a temporal resolution of 6 minutes and a vertical  
 166 resolution of 120 m within the low-level atmosphere. The system incorporates  
 167 advanced signal processing techniques, including ground clutter suppression  
 168 algorithms and adaptive spectral filtering, to mitigate ground clutter interference and  
 169 enhance real-time data fidelity (Solanki et al., 2022; Guo et al., 2023).

170 The L-band radiosonde system delivers high-resolution vertical profiles with a  
 171 temporal resolution of 1 second and a vertical resolution of 5–8 m. Routine observations  
 172 are conducted twice daily at 00 UTC and 12 UTC. The radiosonde data undergo  
 173 rigorous quality control and have been widely used in previous studies to examine  
 174 spatiotemporal variations in turbulence and instability within the free atmosphere and  
 175 PBL (Guo et al., 2016; Lv et al., 2021; Sun et al., 2025). Although horizontal  
 176 displacement occurs between launch sites and balloon trajectories, the spatial



177 exclusivity of these trajectories ensures non-overlapping sampling domains among  
 178 stations. This spatial segregation, combined with high-density vertical profiling,  
 179 enables statistically independent measurements of turbulence-related parameters at  
 180 each station (Ko et al., 2024).

181 Prior to turbulence retrieval through RWP-radiosonde synergetic analysis,  
 182 precipitation events were excluded using ground-based 1-minute precipitation  
 183 observations. Profiles from the RWP and radiosondes were synchronized to a 6-minute  
 184 time resolution, and data collected 30 minutes before and after precipitation events were  
 185 excluded to minimize residual moisture effects on radar refractivity and balloon  
 186 trajectory perturbations (Wu et al., 2024). This rigorous quality assurance process  
 187 yielded 16,942 validated non-precipitation profiles, enabling statistically robust  
 188 characterization of turbulence regimes across China.

## 189 2.2 Algorithms for the estimation of turbulence-related parameters

190 Figure 2 presents the flowchart illustrating the main steps involved in estimating  
 191 the following turbulence-related parameters, squared Brunt–Vaisala frequency ( $N^2$ ),  
 192 turbulence dissipation rate ( $\varepsilon$ ), inner scale ( $l_0$ ), buoyancy length scale ( $L_B$ ), and vertical  
 193 eddy diffusivity ( $K$ ), respectively.

194  $N$  can be estimated based on the pressure and temperature profiles from  
 195 radiosonde measurement (Lilly et al., 1974):

$$N^2 = \frac{g}{\theta} \frac{\partial \theta}{\partial h} \quad (1)$$

196 where  $g$  is the gravitational acceleration,  $\theta$  is the potential temperature as follows:

$$\theta = T \left( \frac{1000}{P} \right)^{0.286} \quad (2)$$

197  $\varepsilon$  is estimated by the Doppler spectral width method (Nanstrom, 1997). Turbulent  
 198 spectral broadening ( $\sigma_{turb}$ ) is quantified by deducting non-turbulent broadening  
 199 components (i.e., beam broadening, shear broadening, and transient effects) from the  
 200 observed spectral width ( $\sigma_{obs}$ ) (Dehghan and Hocking, 2011). The equation is as  
 201 follows:



$$\sigma_{obs}^2 \approx \sigma_{turb}^2 + \sigma_{beam+shear}^2 \quad (3)$$

202  $\sigma_{beam\_shear}^2$  is calculated using the following equations (Dehghan and Hocking,  
 203 2011):

$$\sigma_{beam\_shear}^2 = \frac{\theta_{0.5}^2}{k} u^2 \cos \varphi - a_0 \frac{\theta_{0.5}}{k} \sin \varphi \left( u \frac{\partial u}{\partial z} \zeta \right) + b_0 \frac{2 \sin^2 \varphi}{8k} \left( \frac{\partial u}{\partial z} \zeta \right)^2 \quad (4)$$

$$+ c_0 \sin^2 \varphi \cos^2 \varphi |u \xi| + d_0 \sin^2 \varphi \cos^2 \varphi \xi^2$$

204 where  $k = 4 \ln 2$ ,  $\zeta = 2R\theta_{0.5} \sin \varphi$ ,  $\xi = \frac{\partial u}{\partial z} \frac{\Delta R}{\sqrt{12}}$ ,  $a_0 = 0.945$ ,  $b_0 = 1.500$ ,  $c_0 = 0.030$ ,  
 205  $d_0 = 0.825$ .  $\varphi$  is the beam zenith angle,  $\theta_{0.5}$  is the radar half-power beam width,  $R_0$   
 206 is the radar radial sampling distance,  $\Delta R$  is the radial distance resolution,  $\Delta z$  is the  
 207 vertical resolution,  $u$  is the horizontal wind speed at  $R_0$ , and  $\frac{\partial u}{\partial z}$  is the VWS at  $R_0$ .

208  $\varepsilon$  can be expressed as a function of turbulence-induced spectral broadening  
 209 through the following relationship:

$$\varepsilon = \sigma_{turb}^3 \left( \frac{4\pi}{1.6} \right)^{3/2} J^{-3/2} \quad (5)$$

210  $J$  is computed as follows:

$$J = 12\Gamma\left(\frac{2}{3}\right) \int_0^{\frac{\pi}{2}} d\phi \int_0^{\frac{\pi}{2}} \sin^3 \psi \left( b^2 \cos^2 \psi + a^2 \sin^2 \psi + \frac{L^2}{12} \sin^2 \psi \cos^2 \phi \right)^{\frac{1}{3}} d\psi \quad (6)$$

212 where  $\Gamma$  is the gamma function,  $a$  is the radius of the pulse volume,  $L$  and  $b$  is the half-  
 213 length of the pulse,  $L$  is the product of the mean wind speed and dwell time of the RWP  
 214 during the sampling time, which can be expressed as  $u_t \Delta t$  (Solanki et al., 2022).

215 In the inertial subrange, the scales  $l_0$  and  $L_B$  are the inner and buoyancy length  
 216 scale of turbulence, respectively (Weinstock, 1978; Hocking, 1985).  $L_B$  and  $l_0$  can be  
 217 computed as follows:

$$L_B = \frac{2\pi}{0.62} \left( \frac{\varepsilon}{N^3} \right)^{1/2} \quad (7)$$

$$l_0 = 7.4 \cdot (v^3 / \varepsilon)^{1/4} \quad (8)$$

218 where  $v$  is the kinematic viscosity.

219  $K$  is the ratio of the kinematic heat flux to the mean potential temperature gradient  
 220 (Weinstock, 1981b).  $K$  can be calculated from the following equation:

$$K = \gamma \varepsilon N^{-2} \quad (9)$$

221 where  $\gamma = 0.25$  is the mixing efficiency (Clayson and Kantha, 2008).



## 222 3 Results and discussion

### 223 3.1 Horizontal distribution of turbulence-related parameters

224 The climatological analysis of low-level turbulence regime below 3.0 km AGL  
 225 across China at 00 UTC and 12 UTC in 2023 (Fig. 3) reveals distinct spatial patterns in  
 226 turbulence-related parameters. Those turbulence-related parameters contain squared  
 227 Brunt Vaisalä frequency ( $N^2$ ), gradient Richardson number ( $Ri$ ), turbulence dissipation  
 228 rate ( $\epsilon$ ), vertical eddy diffusivity ( $K$ ), buoyancy length scale ( $L_B$ ), and inner scale ( $l_0$ ).  
 229 To examine the regional changes in above-mentioned turbulence parameters, we  
 230 divided China into four subregions: north China (NC), northwest China (NWC), south  
 231 China (SC) and southwest China (SWC), respectively (Fig. 3a).

232  $N^2$  displays pronounced regional heterogeneity across China, characterized by  
 233 enhanced static stability in SC and diminished stratification in NWC (Figs. 3a and 3b).  
 234 This may be associated with the smaller  $Ri$  in NWC, indicating a more unstable  
 235 atmospheric stratification (Figs. 3a-d). This instability may arise from intensified  
 236 surface-atmosphere interactions driven by the unique environmental conditions over  
 237 NWC, including elevated solar radiation flux due to reduced cloud cover, the  
 238 predominance of bare soil and rock substrates with low albedo, and enhanced sensible  
 239 heat flux from arid landscapes, as compared with those in SC (Xu et al., 2021). As can  
 240 be seen from Figs. 3e and 3f, turbulence is stronger in NC and NWC compared to SC,  
 241 by approximately 1 to 1.5 orders of magnitude, which may be related to stronger  
 242 mechanical driven from VWS and thermally driven convective mixing from surface  
 243 heating (Chen et al., 2022b) (Figs. 3a-3d). The vertical eddy diffusivity  $K$  shows two-  
 244 order amplification in NWC (Figs. 3g-h), governed by the synergistic enhancement of  
 245  $\epsilon$  and  $N^2$  through Equation 9. This contrasts with SC's suppressed turbulence regime,  
 246 where higher vegetation density and moisture increase atmospheric stability (Guo et al.,  
 247 2016; Xu et al., 2021).

248 For the two turbulence scales,  $L_B$  demonstrates inverse spatial patterns compared  
 249 to  $l_0$ .  $L_B$  shows larger values across NC, NWC, and SWC, contrasted by smaller values



in SC. Equation 8 indicates that  $L_B$  is proportional to  $\varepsilon$  and inversely proportional to  $N^3$ , suggesting that smaller  $N^2$  along with larger  $\varepsilon$  contributes to a larger value of  $L_B$ . In contrast,  $l_0$  demonstrates an opposite distribution compared to  $L_B$  (Figs. 3i and 3j). Since  $l_0$  is proportional to  $\rho^3$  and inversely proportional to  $\varepsilon$ , lower  $\rho$  leads to larger  $l_0$  values in SWC. As previously indicated, compared with SC, the strong sensible heat flux in NWC contributes to a more pronounced low-level turbulence characterized by larger  $L_B$  and smaller  $l_0$  values.

Further analysis reveals that the climatological mean values for  $N^2$  are  $10^{-3.76} \text{ s}^{-2}$  at 00 UTC and  $10^{-3.88} \text{ s}^{-2}$  at 12 UTC, while the corresponding values for  $Ri$  are 3.72 and 3.03, indicating greater atmospheric instability at 12 UTC. Under a more unstable atmosphere, turbulence is stronger at 12 UTC, with climatological values of  $10^{-3.37} \text{ m}^2 \text{ s}^{-3}$ ,  $10^{0.72} \text{ m}^2 \text{ s}^{-1}$ , 240.5 m for  $\varepsilon$ ,  $K$  and  $L_B$ , respectively. The enhancement in turbulence metrics at 12 UTC versus 00 UTC baseline originates from the delayed local solar noon in NWC (UTC+6 zones) compared to SC (UTC+8 zones). This leads to stronger turbulence (as shown in Figs. 3f, h) and larger maximum scale of eddy in the inertial subrange (Fig. 3l) in the NWC. Notably, low-level turbulence in SWC at 12 UTC exceeds those values in SC by ~25% (Figs. 3f, h, l), attributable to stronger surface heating over the Tibetan Plateau foothills and Taklamakan Desert.

### 3.2 Vertical structure and probability distribution (PDF) characteristics of turbulence-related parameters

Figures 4a-f show the profiles of  $N^2$ ,  $Ri$ ,  $\varepsilon$ ,  $l_0$ ,  $L_B$ , and  $K$  at 12UTC on 16 July 2023, at Mingfeng in NWC, respectively. It is evident that the vertical structure characteristics of  $N^2$  and  $Ri$  are similar (Figs. 4a and 4b). Below 1.0 km AGL,  $N^2$  is lower than  $10^{-4.60} \text{ s}^{-2}$  (Fig. 4a), and lower gradient Richardson numbers ( $Ri < 0.5$ , Fig. 4b) confirm static instability within low-level atmosphere. In the altitude range from 1.5 to 3.0 km AGL,  $Ri$  exceed 1, suggesting that an increase in static stability is a common feature. As shown in Figs. 4c-4e,  $\varepsilon$ ,  $K$ , and  $L_B$  display consistent vertical structure below 3.0 km, characterized by a pronounced decreasing trend with altitude.  $\varepsilon$  varies from  $10^{-5.2}$  to  $10^{-4.0} \text{ m}^2 \text{ s}^{-3}$  (Fig. 4c), while  $K$  ranges from  $10^{-2.1}$  to  $10^{0.5} \text{ m}^2 \text{ s}^{-1}$



(Fig. 4d) in the low-level atmosphere.  $L_B$  can reach up to about 600 m at 0.5 km but decreases to around 50 m at 3.0 km (Fig. 4e). Conversely,  $l_0$  increased with altitude, ranging from approximately 0.03 m at 0.5 km to about 0.06 m at 3.0 km (Fig. 4f). Reduced stratification  $N^2$  and  $Ri$  synergistically intensify turbulent mixing within the low-level atmosphere and result in larger eddies in the inertial subrange. Furthermore, the intensity of turbulent motions and  $L_B$  diminishes with altitude, while  $l_0$  increases (Ghosh, 2003).

Figure 5 demonstrates the vertical stratification through stability parameters ( $N^2$ ,  $Ri$ ), turbulence characteristics ( $\varepsilon$ ,  $K$ ), and turbulence scale ( $l_0$ ,  $L_B$ ) within the low-level atmosphere in 2023 across China. Below 1.5 km, the values of  $N^2$  and  $Ri$  at 12 UTC are markedly lower than those at 00 UTC (Figs. 5a and 5b), reflecting enhanced atmospheric instability.  $\log_{10}\varepsilon$  shows a nearly linear decrease with increasing altitude below 3.0 km (Fig. 5c), exhibiting gradients of  $-10^{-3.70} \text{ m}^2 \text{ s}^{-3} \text{ km}^{-1}$  at 00 UTC and  $-10^{-3.68} \text{ m}^2 \text{ s}^{-3} \text{ km}^{-1}$  at 12 UTC. This indicates stronger turbulence at lower altitudes, with minimal differences in decay rates. Aligned with  $\varepsilon$ ,  $K$  decreases with altitude at rates of  $-10^{-0.14} \text{ m}^2 \text{ s}^{-1} \text{ km}^{-1}$  (00 UTC) and  $-10^{-0.33} \text{ m}^2 \text{ s}^{-1} \text{ km}^{-1}$  (12 UTC), further supporting reduced turbulent mixing at higher altitudes (Fig. 5d). Larger values of  $L_B$  is observed at lower altitude, while the values of  $l_0$  are larger at higher altitude (Figs. 5e, f) (Ghosh, 2003; Rajput et al., 2022).  $L_B$  decreases sharply with altitude, showing steeper gradients at 12 UTC ( $-180.6 \text{ m km}^{-1}$ ) compared to 00 UTC ( $-69.6 \text{ m km}^{-1}$ ), consistent with stronger turbulence (Fig. 5e). This logarithmic decline suggests rapid attenuation of large turbulent eddies with altitude. In contrast,  $l_0$  increases with altitude at rates of  $0.0083 \text{ m km}^{-1}$  (00 UTC) and  $0.0069 \text{ m km}^{-1}$  (12 UTC), reflecting a shift toward smaller-scale turbulence between the viscous and inertial subranges at higher altitudes (Fig. 5f). Marked vertical variability in buoyancy length and inner scale dynamics reveal turbulence-stratification coupling mechanisms.

Figure 6 presents the PDFs for low-level atmospheric stability parameters ( $N^2$ ,  $Ri$ ), turbulence metrics ( $\varepsilon$ ,  $K$ ), and turbulence scale ( $l_0$ ,  $L_B$ ). It can be observed that  $N^2$  exhibit an approximately Beta-like distribution, with standard deviations of  $10^{-3.72} \text{ s}^{-2}$  at





00 UTC and  $10^{-3.78} \text{ s}^{-2}$  at 12 UTC (Fig. 6a).  $Ri$  displays characteristics of an approximate Gamma distribution (Fig. 6b), consistent with its sensitivity to shear-driven instabilities. Both  $\varepsilon$  and  $K$  show traits typical of log-normal distributions (Rajput et al., 2022), with standard deviations of  $10^{-3.11} \text{ m}^2 \text{ s}^{-3}$  ( $10^{-3.07} \text{ m}^2 \text{ s}^{-3}$ ) for  $\varepsilon$ , and  $10^{0.93} \text{ m}^2 \text{ s}^{-1}$  ( $10^{1.09} \text{ m}^2 \text{ s}^{-1}$ ) for  $K$  at 00UTC (12UTC), respectively (Figs. 6c-d). For the horizontal turbulence scale sizes,  $l_0$  and  $L_B$  exhibit approximate Gamma distributions (Figs. 6e and 6f).  $l_0$  exhibits standard deviations of 0.013 m (0.012 m) at 00 UTC (12 UTC), respectively.  $L_B$  displays larger variability deviations of 219.8 m (264.1 m) at 00 UTC (12 UTC), respectively. The distinct PDF shapes reflect fundamental differences in the statistical behavior of stability, turbulence, and mixing parameters. The near log-normal distributions of  $\varepsilon$  and  $K$  suggest Gaussian-like randomness in turbulent processes, while the Gamma and Beta-like distributions of  $Ri$  and  $N^2$  align with their dependency on threshold-governed instabilities.

Figure 7 demonstrates the relationships among turbulence-related parameters, with their quantitative correlation coefficients systematically presented at 00 UTC and 12 UTC, respectively. Notably,  $\text{Log}_{10}N^2$  and  $Ri$  exhibit strong covariation, reflecting progressive stratification breakdown during atmospheric destabilization. The correlation coefficients for  $\text{Log}_{10}\varepsilon$  with  $\text{Log}_{10}N^2$  at 00 UTC (Fig. 7a) and 12 UTC (Fig. 7b) are -0.19 and -0.13, while the coefficients with  $Ri$  are -0.22 and -0.12, respectively. These values suggest that turbulence tends to be stronger in unstable atmospheric regimes.  $\text{Log}_{10}K$  demonstrates robust covariance with  $\text{Log}_{10}\varepsilon$  ( $R > 0.80$ ), whereas inverse mechanistic linkages emerge stability indices ( $\text{Log}_{10}N^2$  and  $Ri$ ).  $L_B$  exhibits divergent relationships, showing positive correlations with turbulent metrics ( $R > 0.65$  with  $\text{Log}_{10}\varepsilon$  and  $\text{Log}_{10}K$ ), while displaying inverse correlations with stability indices ( $R < -0.45$  with  $\text{Log}_{10}N^2$  and  $Ri$ ). The characteristic inner scale  $l_0$  shows an inverse pattern to  $L_B$ , with negative correlations to  $\text{Log}_{10}\varepsilon$  ( $R < -0.80$ ) and  $\text{Log}_{10}K$  ( $R < -0.6$ ), but positive correlations with  $\text{Log}_{10}N^2$  and  $Ri$ . The interaction manifests as a marked negative correlation between  $L_B$  and  $l_0$ , with statistical confirmation of their anticorrelation pattern. These systematic correlations collectively suggest that



atmospheric stability of stratification in the buoyancy subrange fundamentally modulate turbulent cascades and energy transfer processes through their coordinated effects on both buoyancy-dominated and shear-driven turbulent structures (Lotfy et al., 2019; Rajput et al., 2022).

### 3.3 Seasonal variation of turbulence-related parameters with atmospheric stability

The previous subsection analyzed the spatial distribution and vertical structure of climatological turbulence-related parameters across China. This subsection focuses on the temporal turbulent variation in low-level atmosphere.

Figures. 8-9 systematically delineates interannual variability and seasonal cyclic patterns of  $N^2$ ,  $Ri$ ,  $\varepsilon$ ,  $l_0$ ,  $L_B$ , and  $K$ .  $N^2$  is lower in spring and summer, but higher in autumn and winter, indicating greater atmospheric instability during warmer months (Figs. 8a and 8b). In summer,  $N^2$  reaches its minimum below 1.2 km, indicating a more unstable stratification. Both  $\varepsilon$  and  $K$  exhibit higher values in spring and summer, and lower values in autumn and winter, with an approximate increase of one order of magnitude during warmer seasons (Chen et al., 2022a) (Figs. 8c-f).  $L_B$  follows a similar seasonal pattern to  $\varepsilon$  and  $K$  (Figs. 8i-j), further supporting the link between turbulence intensity and turbulence scales in the buoyancy subrange. In contrast, the annual evolution of  $l_0$  (Figs. 8g and 8h) is inversely related to  $\varepsilon$  and  $K$ , with smaller values in spring and summer and larger values in autumn and winter (Figs. 8g, 8h). The vertical profiles of  $\varepsilon$ ,  $K$ , and  $L_B$  consistently decrease with altitude across all seasons, highlighting the altitude-dependent characteristics of turbulent processes.

The seasonal evolutions of  $\varepsilon$  at 00 UTC and 12 UTC are broadly similar, though  $\varepsilon$  is consistently stronger at 12 UTC, likely due to lower values of  $N^2$  and  $Ri$  (Figs. 8a-b). In summer at 12 UTC,  $\varepsilon$  exceeds  $10^{-3.5} \text{ m}^2 \text{ s}^{-3}$  at an altitude of 1.8 km, whereas in winter, this altitude is only reached at 0.6 km. This highlights the influence of seasonal turbulent dynamics on the development of the PBL. This suggests the existence of a maximum descent gradient region for  $\varepsilon$  and  $K$  at the PBL top (Meng et al., 2024). At 12 UTC, the  $l_0$  values at 0.5 km are 0.012 m in summer and 0.013 m in winter, while



at 1.2 km, those values are 0.021 m in summer and 0.024 m in winter, respectively (Fig. 8i). The values of  $L_B$  at 12 UTC are 910 m in summer and 550 m in winter at an altitude of 0.5 km, respectively (Fig. 8j). At 1.2 km, the values of  $L_B$  are 570 m in summer and 300 m in winter, respectively, which is approximately half of the values observed at 0.5 km. The seasonal variations in turbulence parameters underscore the critical role of atmospheric stability and PBL processes in modulating low-level turbulence intensity and mixing.

As previously discussed, the low-level atmosphere at 12 UTC exhibits greater instability compared to 00 UTC, resulting in stronger turbulence. However, it should be noted that 12 UTC corresponds to local standard time between 18 and 20 LST, during which the PBL may exist in either a mixed or transitional state (Guo et al., 2016). To further investigate the relationship between turbulence structure and atmospheric stability at 12 UTC, this study adopted  $Ri < 0.25$  as an indicator of atmospheric instability (Chen et al., 2022a).

Figure 10 shows the vertical and seasonal distribution frequency of  $Ri < 0.25$  at 00 UTC and 12 UTC. A distinct seasonal variation in the occurrence frequency is observed. Analysis of the occurrence frequency climatology reveals pronounced seasonality in low-level instability, with peak intensity occurring and maximum eddies ( $L_B \approx 573.9$  m) at 12 UTC in May during the spring-summer transition period dominated by enhanced thermal convection and synoptic-scale frontal activity (Chen et al., 2022a). This seasonal maximum coincides with weakened static stability and enhanced turbulence (Fig. 8), facilitating vigorous vertical mixing through buoyancy-driven plumes. Conversely, autumn-winter months exhibit suppressed turbulence and smaller buoyancy length scale (minimum  $L_B \approx 272.6$  m in January), corresponding to increased atmospheric stratification and reduced surface heat fluxes under frequent temperature inversion regimes (Xu et al., 2021).

Furthermore, a significant discrepancy exists between the occurrence frequency of  $Ri < 0.25$  at 00 UTC and 12 UTC. For instance, in May, the vertical mean frequency of  $Ri < 0.25$  at 12 UTC is 23.6%, whereas at 00 UTC it registers only 14.9%. This disparity



indicates a more unstable atmosphere and stronger turbulence at 12 UTC (Figs. 6d and 8c-f). Vertically, the frequency exhibits a decreasing trend with altitude, suggesting that the vertical structure of atmospheric instability contributes to the height-dependent attenuation of turbulence intensity (Figs. 5c-d and 8c-f).

Figure 11 presents the vertical structural distribution of correlations among turbulence-related parameters.  $\log_{10}\epsilon$  show positive correlations with occurrence frequency of  $Ri < 0.25$  across altitudes (Fig. 11a), though  $\log_{10}K$  exhibits stronger correlations (not shown). This indicates that vertical eddy diffusivity responds more sensitively to unstable atmospheric instability, particularly at 12 UTC where the correlation coefficient exceeds 0.5 at 1~2 km AGL. As shown in Fig. 11b,  $l_0$  demonstrates significant negative correlations ( $R < -0.9$ ) with  $\log_{10}\epsilon$  vertically, suggesting that enhanced turbulence under lower atmospheric instability corresponds to smaller  $l_0$  between the viscous and inertial subranges (Fig. 11b). Conversely,  $L_B$  show significant positive correlations with both  $\log_{10}\epsilon$ , implying that stronger turbulence enlarges the maximum turbulent eddies between the inertial and buoyancy subranges (Fig. 11c). The correlation between  $l_0$  and  $L_B$  is more pronounced at lower altitudes but remains relatively stable above 1 km. Hence, when the instability of the low-level atmosphere increases, the enhanced turbulence expands the range of the inertial subrange (Rajput et al., 2022).

## 4 Summary and concluding remarks

The estimation of turbulence-related parameters can help improving the accuracy of short-term local weather forecasts. Despite its importance, detailed research on the structure of low-level atmospheric turbulence has been hindered by a lack of comprehensive observational data. This study aims to address this gap by investigating the temporal and spatial evolution patterns of low-level turbulence in China.

Using observational data from 29 co-located RWP and radiosonde stations across China, this research employs the Doppler spectrum width method to estimate critical parameters of lower-level atmospheric turbulence. These parameters include the



squared Brunt–Vaisala frequency ( $N^2$ ), turbulent dissipation rate ( $\varepsilon$ ), inner scale ( $l_0$ ), buoyancy length scale ( $L_B$ ), and vertical eddy diffusivity ( $K$ ). A comprehensive dataset of turbulence-related parameters was developed at the station scale for China in 2023, with a temporal resolution of 6-minute and a vertical resolution of 120 m below 3.0 km AGL.

Spatially, low-level turbulence demonstrates significant geographical variability. Compared to south China (SC),  $N^2$  and  $l_0$  are lower in northwest China (NWC) and north China (NC), while  $\varepsilon$ ,  $L_B$ , and  $K$  are higher. This indicates stronger turbulence in the NWC and NC. It can be concluded that the predominance of bare land with low soil moisture in NWC and NC results in higher sensible heat flux, promoting greater heat transfer to the PBL, more unstable atmospheric stratification, and stronger turbulence compared to the forested, high soil moisture regions of SC.

As altitude increases,  $\varepsilon$ ,  $L_B$ , and  $K$  exhibit a decreasing trend, while  $N^2$  and  $l_0$  increase. The PDF of  $\varepsilon$  and  $K$  conform a log-normal distribution, whereas  $l_0$  and  $L_B$  approximately follow a Gamma distribution. Temporally, turbulence-related parameters display pronounced seasonal variations, with stronger turbulence observed in spring and summer and weaker turbulence in autumn and winter. Additionally, turbulence intensity at 12 UTC is notably stronger than at 00 UTC, primarily due to the unstable atmospheric stratification with a larger occurrence frequency of  $Ri < 0.25$ .

Although the dataset of low-level atmospheric turbulence-related parameters developed in this study encompasses typical regions across China, the limited station density and sparse radiosonde observations constrain the dataset's ability to provide high spatiotemporal resolution turbulence profiles for the entire country. In future work, additional data sources, such as coherent Doppler wind lidars and reanalysis datasets, will be integrated to construct a more refined, grid-scale turbulence dataset for China, enabling a more comprehensive understanding of atmospheric turbulence dynamics.

## Author contributions

JG designed the research framework and conceptualized this study; DM and JG



451 conducted the experiment and drafted the initial manuscript; XG, NL and NT helped  
 452 the data collection and carried out the quality control. YS and ZZ prepared all  
 453 distributed turbulence-related datasets. JC, HX, TC, JH and RY contributed to the  
 454 revision of the manuscript. All authors contributed to writing and reviewing the paper.

## 455 **Competing interests**

456 The contact author has declared that there are no competing interests for all authors.

## 457 **Financial support**

458 This manuscript was jointly under the auspices of the National Natural Science  
 459 Foundation of China under grants of 42325501, the Chinese Academy of  
 460 Meteorological Sciences under grant 2024Z003 and the Department of Science and  
 461 Technology of Guizhou province under grant KXJZ [2024] 033. the CMA Xiong'an  
 462 Atmospheric Boundary Layer Key Laboratory under grant of 2023LABL-B06.

## 463 **Data availability**

464 The low-level turbulence-related dataset in China can be accessed at  
 465 <https://doi.org/10.5281/zenodo.14959025> (Meng and Guo, 2025).

## 466 **References**

- 467 Brunke, M. A., Cutler, L., Urzua, R. D., Corral, A. F., Crosbie, E., Hair, J., Hostetler,  
 468 C., Kirschler, S., Larson, V., Li, X. Y., Ma, P. L., Minke, A., Moore, R., Robinson,  
 469 C. E., Scarino, A. J., Schlosser, J., Shook, M., Sorooshian, A., Thornhill, K. L., Voigt,  
 470 C., Wan, H., Wang, H. L., Winstead, E., Zeng, X. B., Zhang, S. X., and Ziemba, L.  
 471 D.: Aircraft observations of turbulence in cloudy and cloud-free boundary layers  
 472 over the western north Atlantic ocean from ACTIVATE and implications for the earth  
 473 system model evaluation and development, *Journal of Geophysical Research-*  
 474 *Atmospheres*, 127, 24, 10.1029/2022jd036480, 2022.
- 475 Chechin, D. G., Lüpkes, C., Hartmann, J., Ehrlich, A., and Wendisch, M.: Turbulent  
 476 structure of the Arctic boundary layer in early summer driven by stability, wind shear



- 477 and cloud-top radiative cooling: ACLOUD airborne observations, *Atmospheric*  
 478 *Chemistry and Physics*, 23, 4685-4707, 10.5194/acp-23-4685-2023, 2023.
- 479 Chen, Z., Tian, Y. F., and Lue, D. R.: Turbulence parameters in the troposphere-lower  
 480 stratosphere observed by Beijing MST radar, *Remote Sensing*, 14, 18,  
 481 10.3390/rs14040947, 2022a.
- 482 Chen, Z., Tian, Y. F., and Lue, D. R.: Turbulence parameters in the troposphere-lower  
 483 stratosphere observed by beijing mst radar, *Remote Sensing*, 14, 18,  
 484 10.3390/rs14040947, 2022b.
- 485 Clayson, C. A. and Kantha, L.: On turbulence and mixing in the free atmosphere  
 486 inferred from high-resolution soundings, *Journal of Atmospheric and Oceanic*  
 487 *Technology*, 25, 833-852, 10.1175/2007jtecha992.1, 2008.
- 488 Cohn, S. A.: Radar Measurements of Turbulent eddy dissipation rate in the troposphere  
 489 a comparison of techniques, *Journal of Atmospheric and Oceanic Technology*, 12,  
 490 85-95, 10.1175/1520-0426(1995)012<0085:Rmoted>2.0.Co;2, 1995.
- 491 Dehghan, A. and Hocking, W. K.: Instrumental errors in spectral-width turbulence  
 492 measurements by radars, *Journal of Atmospheric and Solar-Terrestrial Physics*, 73,  
 493 1052-1068, 10.1016/j.jastp.2010.11.011, 2011.
- 494 Eaton, F. D. and Nastrom, G. D.: Preliminary estimates of the vertical profiles of inner  
 495 and outer scales from White Sands Missile Range, New Mexico, VHF radar  
 496 observations, *Radio Sci.*, 33, 895-903, 10.1029/98rs01254, 1998.
- 497 Fukao, S., Yamanaka, M. D., Ao, N., Hocking, W. K., Sato, T., Yamamoto, M.,  
 498 Nakamura, T., Tsuda, T., and Kato, S.: Seasonal variability of vertical eddy  
 499 diffusivity in the middle atmosphere 1. Three-year observations by the middle and  
 500 upper atmosphere radar, *Journal of Geophysical Research-Atmospheres*, 99, 18973-  
 501 18987, 10.1029/94jd00911, 1994.
- 502 Gage, K. S. and Balsley, B. B.: Doppler radar probing of the clear atmosphere, *Bulletin*  
 503 *of the American Meteorological Society*, 59, 1074-1093, 10.1175/1520-  
 504 0477(1978)059<1074:Drpote>2.0.Co;2, 1978.
- 505 Ghosh, A. K., Jain, A. R., and Sivakumar, V.: Simultaneous MST radar and radiosonde  
 506 measurements at Gadanki (13.5°N, 79.2°E) -: 2.: Determination of various  
 507 atmospheric turbulence parameters -: art. no. 1014, *Radio Sci.*, 38, 12,  
 508 10.1029/2000rs002528, 2003.
- 509 Guo, J. P., Miao, Y. C., Zhang, Y., Liu, H., Li, Z. Q., Zhang, W. C., He, J., Lou, M. Y.,  
 510 Yan, Y., Bian, L. G., and Zhai, P.: The climatology of planetary boundary layer height  
 511 in China derived from radiosonde and reanalysis data, *Atmospheric Chemistry and*  
 512 *Physics*, 16, 13309-13319, 10.5194/acp-16-13309-2016, 2016.
- 513 Hocking, W. K.: Measurement of turbulent energy dissipation rates in the middle  
 514 atmosphere by radar techniques A review, *Radio Sci.*, 20, 1403-1422,



- 10.1029/RS020i006p01403, 1985.
- Hocking, W. K. and Mu, P. K. L.: Upper and middle tropospheric kinetic energy dissipation rates from measurements of  $(C_n^2)$  - review of theories, in-situ investigations, and experimental studies using the Buckland Park atmospheric radar in Australia, *Journal of Atmospheric and Solar-Terrestrial Physics*, 59, 1779-1803, 10.1016/s1364-6826(97)00020-5, 1997.
- Jacoby-Koaly, S., Campistron, B., Bernard, S., Bénech, B., Girard-Ardhuin, F., Dessens, J., Dupont, E., and Carissimo, B.: Turbulent dissipation rate in the boundary layer via UHF wind profiler Doppler spectral width measurements, *Bound.-Layer Meteor.*, 103, 361-389, 10.1023/a:1014985111855, 2002.
- Jaiswal, A., Phanikumar, D. V., Bhattacharjee, S., and Naja, M.: Estimation of turbulence parameters using ariess radar and gps radiosonde measurements: first results from the central himalayan region, *Radio Sci.*, 55, 18, 10.1029/2019rs006979, 2020.
- Ko, H. C., Chun, H. Y., Geller, M. A., and Ingleby, B.: Global distributions of atmospheric turbulence estimated using operational high vertical-resolution radiosonde data, *Bulletin of the American Meteorological Society*, 105, E2551-E2566, 10.1175/bams-d-23-0193.1, 2024.
- Kohma, M., Sato, K., Tomikawa, Y., Nishimura, K., and Sato, T.: Estimate of turbulent energy dissipation rate from the VHF radar and radiosonde observations in the Antarctic, *Journal of Geophysical Research-Atmospheres*, 124, 2976-2993, 10.1029/2018jd029521, 2019.
- Li, Q., Rapp, M., Schrön, A., Schneider, A., and Stober, G.: Derivation of turbulent energy dissipation rate with the Middle Atmosphere Alomar Radar System (MAARSY) and radiosondes at Andoya, Norway, *Ann. Geophys.*, 34, 1209-1229, 10.5194/angeo-34-1209-2016, 2016.
- Lilly, D. K., Waco, D. E., and Adelfang, S. I.: Stratospheric mixing estimated from high-altitude turbulence measurements, *J. Appl. Meteorol.*, 13, 488-493, 10.1175/1520-0450(1974)013<0488:Smefha>2.0.Co;2, 1974.
- Lotfy, E. R., Abbas, A. A., Zaki, S. A., and Harun, Z.: Characteristics of turbulent coherent structures in atmospheric flow under different shear-buoyancy conditions, *Bound.-Layer Meteor.*, 173, 115-141, 10.1007/s10546-019-00459-y, 2019.
- Luce, H., Kantha, L., and Hashiguchi, H.: Statistical assessment of a Doppler radar model of TKE dissipation rate for low Richardson numbers, *Atmospheric Measurement Techniques*, 16, 5091-5101, 10.5194/amt-16-5091-2023, 2023a.
- Luce, H., Kantha, L., Hashiguchi, H., Lawrence, D., Doddi, A., Mixa, T., and Yabuki, M.: Turbulence kinetic energy dissipation rate: assessment of radar models from comparisons between 1.3 GHz wind profiler radar (WPR) and DataHawk UAV





- 553 measurements, *Atmospheric Measurement Techniques*, 16, 3561-3580,  
 554 10.5194/amt-16-3561-2023, 2023b.
- 555 Lv, Y. M., Guo, J. P., Li, J., Cao, L. J., Chen, T. M., Wang, D., Chen, D. D., Han, Y.,  
 556 Guo, X. R., Xu, H., Liu, L., Solanki, R., and Huang, G.: Spatiotemporal  
 557 characteristics of atmospheric turbulence over China estimated using operational  
 558 high-resolution soundings, *Environmental Research Letters*, 16, 13, 10.1088/1748-  
 559 9326/abf461, 2021.
- 560 Muñoz-Esparza, D., Sharman, R. D., and Lundquist, J. K.: Turbulence dissipation rate  
 561 in the atmospheric boundary layer: observations and WRF mesoscale modeling  
 562 during the XPIA field campaign, *Monthly Weather Review*, 146, 351-371,  
 563 10.1175/mwr-d-17-0186.1, 2018.
- 564 Marquis, J. N., Varble, A. C., Robinson, P., Nelson, T. C., and Friedrich, K.: Low-level  
 565 mesoscale and cloud-scale interactions promoting deep convection initiation,  
 566 *Monthly Weather Review*, 149, 2473-2495, 10.1175/mwr-d-20-0391.1, 2021.
- 567 Namboodiri, K. V. S., Dileep, P. K., Mammen, K., Ramkumar, G., Kumar, N.,  
 568 Sreenivasan, S., Kumar, B. S., and Manchanda, R. K.: Effects of annular solar eclipse  
 569 of 15 January 2010 on meteorological parameters in the 0 to 65 km region over  
 570 Thumba, India, *Meteorol. Z.*, 20, 635-647, 10.1127/0941-2948/2011/0253, 2011.
- 571 Nicholls, S.: The dynamics of stratocumulus Aircraft observations and comparisons  
 572 with a mixed layer model, *Quarterly Journal of the Royal Meteorological Society*,  
 573 110, 783-820, 10.1002/qj.49711046603, 1984.
- 574 Nowak, J. L., Siebert, H., Szodry, K. E., and Malinowski, S. P.: Coupled and decoupled  
 575 stratocumulus-topped boundary layers: turbulence properties, *Atmospheric  
 576 Chemistry and Physics*, 21, 10965-10991, 10.5194/acp-21-10965-2021, 2021.
- 577 Meng, D., Guo, J.: A low-level turbulence-related parameters dataset derived from the  
 578 radar wind profiler and radiosonde in China during 2023. [Data  
 579 set]. <https://doi.org/10.5281/zenodo.14959025>, 2025.
- 580 Meng, D. L., Guo, J. P., Guo, X. R., Wang, Y. J., Li, N., Sun, Y. P., Zhang, Z., Tang, N.,  
 581 Li, H. R., Zhang, F., Tong, B., Xu, H., and Chen, T. M.: Elucidating the boundary  
 582 layer turbulence dissipation rate using high-resolution measurements from a radar  
 583 wind profiler network over the Tibetan Plateau, *Atmospheric Chemistry and Physics*,  
 584 24, 8703-8720, 10.5194/acp-24-8703-2024, 2024.
- 585 Nastrom, G. D.: Doppler radar spectral width broadening due to beamwidth and wind  
 586 shear, *Ann. Geophys.-Atmos. Hydrospheres Space Sci.*, 15, 786-796,  
 587 10.1007/s00585-997-0786-7, 1997.
- 588 Nastrom, G. D. and Eaton, F. D.: A brief climatology of eddy diffusivities over White  
 589 Sands Missile Range, New Mexico, *Journal of Geophysical Research-Atmospheres*,  
 590 102, 29819-29826, 10.1029/97jd02208, 1997.



- 591 Rajput, A., Singh, N., Singh, J., and Rastogi, S.: Investigation of atmospheric  
 592 turbulence and scale lengths using radiosonde measurements of GVAX-campaign  
 593 over central Himalayan region, *Journal of Atmospheric and Solar-Terrestrial Physics*,  
 594 235, 16, 10.1016/j.jastp.2022.105895, 2022.
- 595 Satheesan, K. and Murthy, B. V. K.: Turbulence parameters in the tropical troposphere  
 596 and lower stratosphere, *Journal of Geophysical Research-Atmospheres*, 107, 13,  
 597 10.1029/2000jd000146, 2002.
- 598 Sato, T. and Woodman, R. F.: Fine altitude resolution observations of stratospheric  
 599 turbulent layers by the Arecibo 430-MHz radar, *Journal of the Atmospheric Sciences*,  
 600 39, 2546-2552, 10.1175/1520-0469(1982)039<2546:Faroos>2.0.Co;2, 1982.
- 601 Shelekhov, A. P., Afanasiev, A. L., Shelekhova, E. A., Kobzev, A. A., Tel'minov, A. E.,  
 602 Molchunov, A. N., and Poplevina, O. N.: Using small unmanned aerial vehicles for  
 603 turbulence measurements in the atmosphere, *Izv. Atmos. Ocean. Phys.*, 57, 533-545,  
 604 10.1134/s0001433821050133, 2021.
- 605 Solanki, R., Guo, J. P., Lv, Y. M., Zhang, J., Wu, J. Y., Tong, B., and Li, J.: Elucidating  
 606 the atmospheric boundary layer turbulence by combining UHF radar wind profiler  
 607 and radiosonde measurements over urban area of Beijing, *Urban CLim.*, 43, 13,  
 608 10.1016/j.uclim.2022.101151, 2022.
- 609 Sun, Y., Guo J., Chen T., Li N., Guo X., Xu H., Zhang Z., Shi Y., Zeng L., Chen J.,  
 610 Meng D.: Long-term high-resolution radiosonde measurements reveal more  
 611 intensified and frequent turbulence at cruising altitude in China, *Geophys. Res. Lett.*,  
 612 52, e2024GL114076, /10.1029/ 2024GL114076, 2025.
- 613 Thorpe, S. A.: Turbulence and mixing in a Scottish Loch, *Philos. Trans. R. Soc. A-Math.*  
 614 *Phys. Eng. Sci.*, 286, 125-181, 10.1098/rsta.1977.0112, 1977.
- 615 Weinstock, J.: Vertical turbulent diffusion in a stably stratified fluid, *Journal of the*  
 616 *Atmospheric Sciences*, 35, 1022-1027, 10.1175/1520-  
 617 0469(1978)035<1022:Vtdias>2.0.Co;2, 1978.
- 618 Weinstock, J.: Using radar to estimate dissipation rates in thin layers of turbulence,  
 619 *Radio Sci.*, 16, 1401-1406, 10.1029/RS016i006p01401, 1981a.
- 620 Weinstock, J.: Vertical turbulence diffusivity for weak or strong stable stratification,  
 621 *Journal of Geophysical Research-Oceans*, 86, 9925-9928,  
 622 10.1029/JC086iC10p09925, 1981b.
- 623 Wilson, R.: Turbulent diffusivity in the free atmosphere inferred from MST radar  
 624 measurements: a review, *Ann. Geophys.*, 22, 3869-3887, 10.5194/angeo-22-3869-  
 625 2004, 2004.
- 626 Wilson, R., Luce, H., Hashiguchi, H., Nishi, N., and Yabuki, Y.: Energetics of persistent  
 627 turbulent layers underneath mid-level clouds estimated from concurrent radar and  
 628 radiosonde data, *Journal of Atmospheric and Solar-Terrestrial Physics*, 118, 78-89,



629      10.1016/j.jastp.2014.01.005, 2014.  
630      Wu, J. Y., Guo, J. P., Yun, Y. X., Yang, R. F., Guo, X. R., Meng, D. L., Sun, Y. P., Zhang,  
631      Z., Xu, H., and Chen, T. M.: Can ERA5 reanalysis data characterize the pre-storm  
632      environment? *Atmospheric Research*, 297, 18, 10.1016/j.atmosres.2023.107108,  
633      2024.  
634      Xu, Z. Q., Chen, H. S., Guo, J. P., and Zhang, W. C.: Contrasting effect of soil moisture  
635      on the daytime boundary layer under different thermodynamic conditions in summer  
636      over China, *Geophysical Research Letters*, 48, 11, 10.1029/2020gl090989, 2021.



**Table 1.** Summary of the radar wind profiler (RWP) stations used in the calculation of turbulence related parameters.

ID	Station	Lon. (°E)	Lat. (°N)	Elevation (m)
50953	Harbin	126.58	45.93	115.0
51463	Urumqi	87.74	43.81	935.0
51839	Minfeng	82.69	37.07	1408.9
52533	Jiuquan	98.49	39.77	1477.2
53463	Hohhot	111.57	40.86	1152.1
53772	Taiyuan	112.58	37.62	785.0
53845	Yan'an	109.45	36.58	1180.4
54304	Zhangjiakou	115.27	40.95	726.0
54511	Beijing	116.47	39.81	31.5
54727	Zhangqiu	117.52	36.65	251.9
55664	Tingri	87.12	28.65	4326.8
56029	Yushu	96.96	33.00	3684.0
56146	Ganzi	100.00	31.62	3353.0
56173	Hongyuan	102.55	32.79	3465.0
56312	Linzhi	94.36	29.65	2988.4
56651	Lijiang	100.22	26.85	2382.4
56964	Simao	100.99	22.82	1423.3
57461	Sanxia	111.36	30.74	253.8
57516	Chongqing	106.46	29.58	260.0
57687	Changsha	112.79	28.11	46.0
57816	Guiyang	106.73	26.59	1223.7
58238	Nanjing	118.90	31.93	40.6
58459	Hangzhou	120.29	30.18	43.0
58633	Quzhou	118.89	28.99	86.4
58725	Shaowu	117.50	27.31	363.6
58847	Fuzhou	119.29	26.08	112.1
59312	Chaozhou	116.69	23.67	7.0
59431	Nanning	108.55	22.78	104.9
59758	Haikou	110.25	19.99	69.0



## Figures

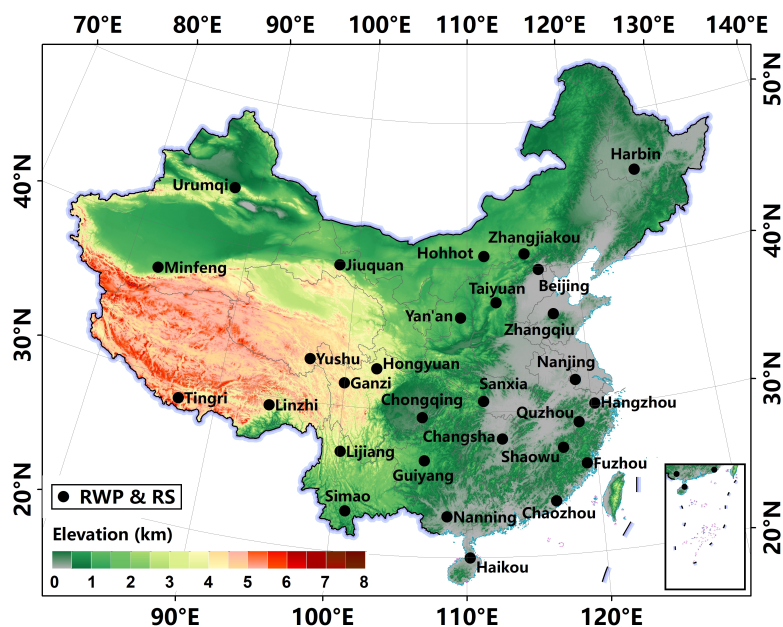
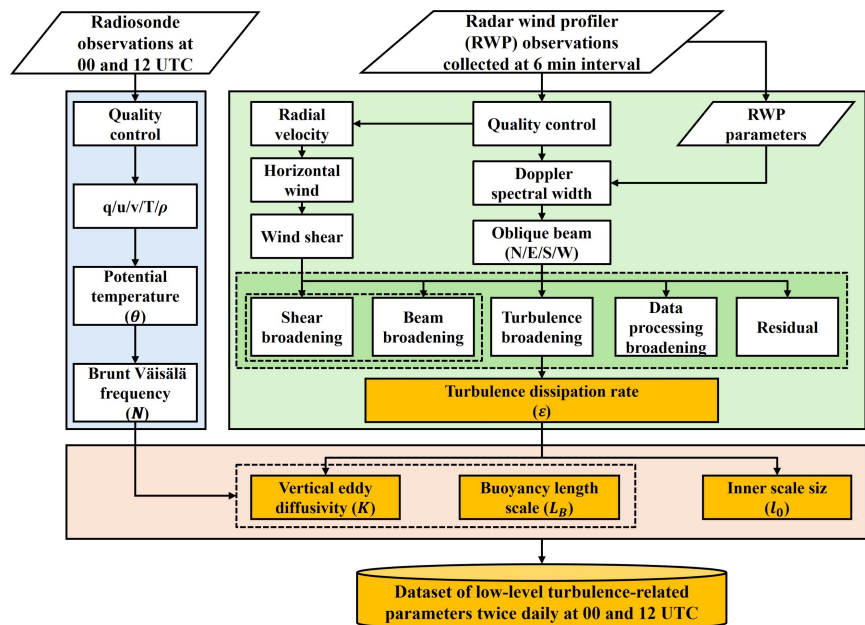


**Figure 1.** Spatial distribution of the co-located radar wind profiler (RWP) and radiosonde stations in China.



645



646

647 **Figure 2.** Flowchart used to generate the low-level atmospheric turbulence-related  
 648 dataset at 00 UTC and 12 UTC in China. Turbulence-related parameters include squared  
 649 Brunt Väisälä frequency ( $N^2$ ), turbulent dissipation rate ( $\epsilon$ ), inner scale ( $l_0$ ), buoyancy  
 650 length scale ( $L_B$ ), vertical eddy diffusivity ( $K$ ), respectively.

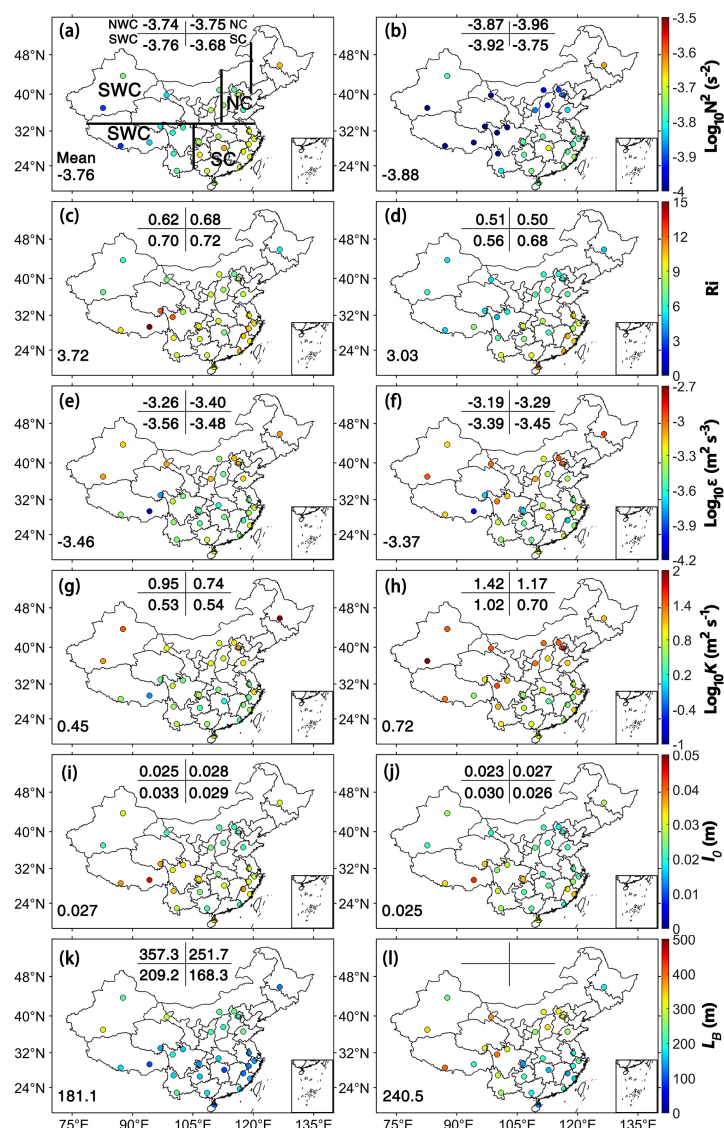
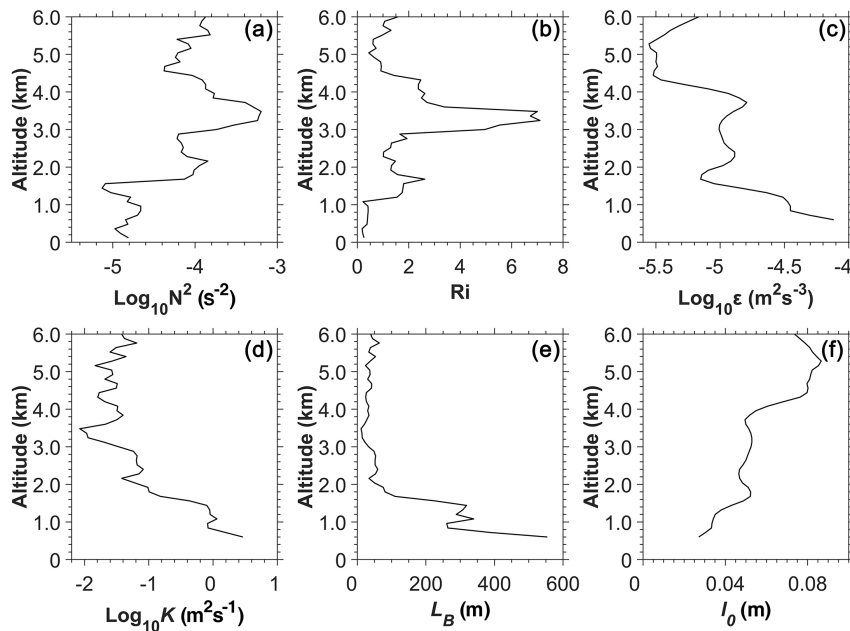
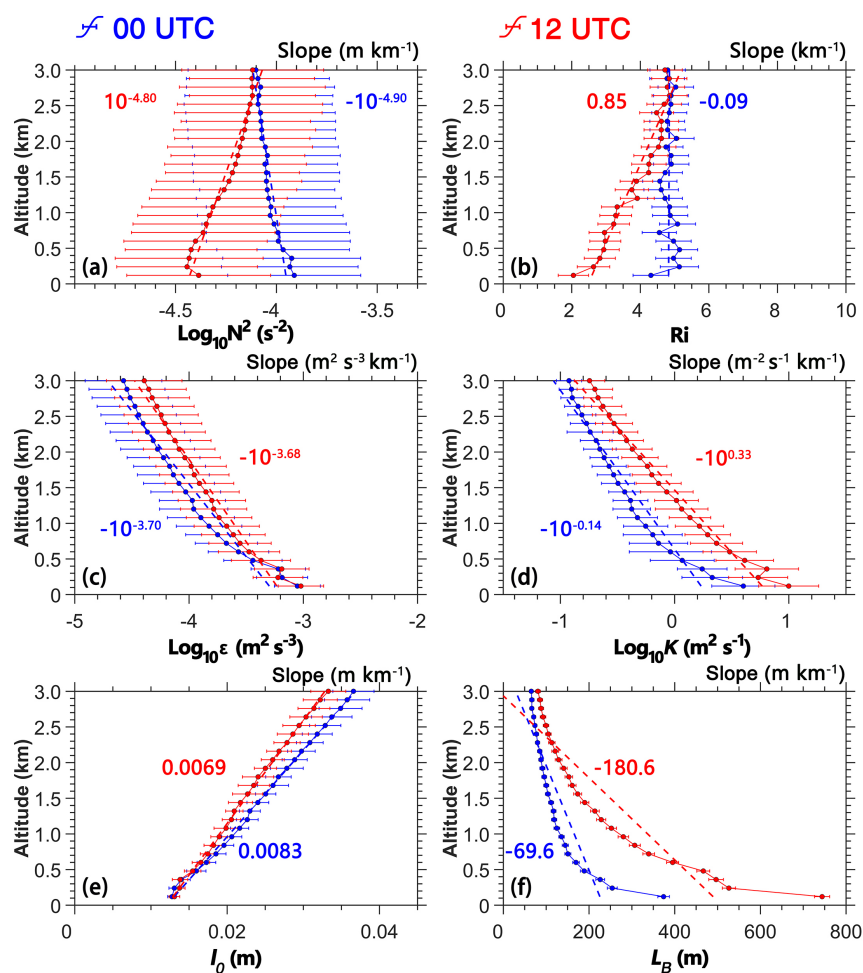


**Figure 3.** Spatial distribution and mean values of squared Brunt-Vaisälä frequency ( $N^2$ ) below 3.0 km above ground level (AGL) for 2023 at (a) 00 UTC and (b) 12 UTC, (c, d) Richardson number ( $Ri$ ), (e, f) turbulent dissipation rate ( $\epsilon$ ), (g, h) vertical eddy diffusivity ( $K$ ), (i, j) inner scale ( $l_0$ ), (k, l) buoyancy length scale ( $L_B$ ), respectively. Here, China is divided into four subregions, north China (NC), northwest China (NWC), south China (SC) and southwest China (SWC), respectively.



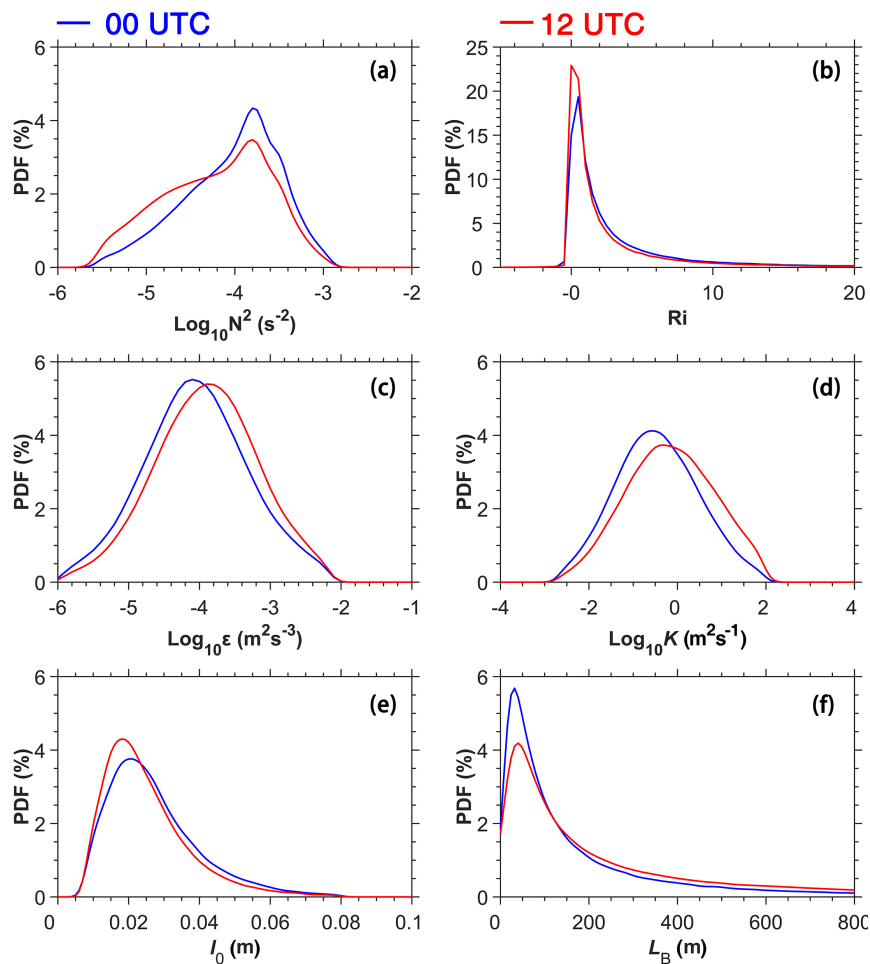
658  
 659 **Figure 4.** Vertical profiles of (a) squared Brunt Vaisalä frequency ( $N^2$ ), (b) Richardson  
 660 number ( $Ri$ ), (c) turbulence dissipation rate ( $\epsilon$ ), (d) vertical eddy diffusivity ( $K$ ), (e)  
 661 buoyancy length scale ( $L_B$ ) and (f) inner scale ( $l_0$ ) at 12 UTC for 16 July 2023 at  
 662 Minfeng in northwest China. Note that  $N^2$  is deduced from the sorted potential  
 663 temperature ( $\theta$ ), it shows no regions of negative stability, however,  $Ri$  is inferred from  
 664 the unsorted  $\theta$  profile.  
 665



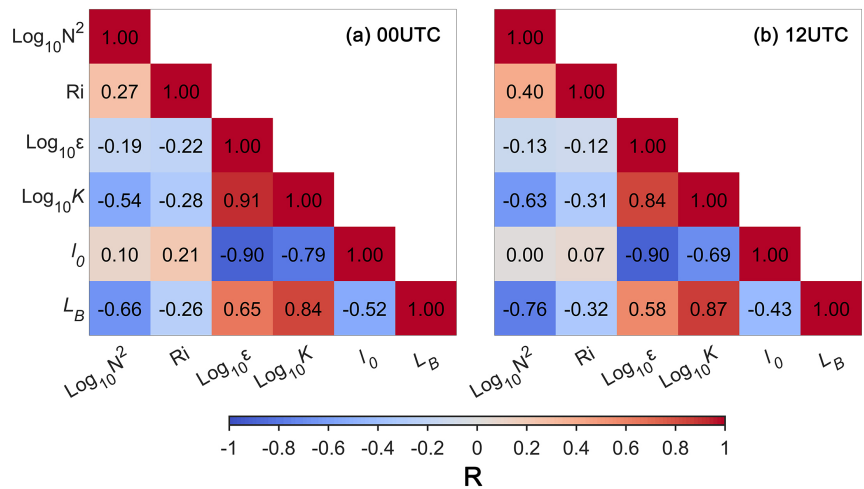


666

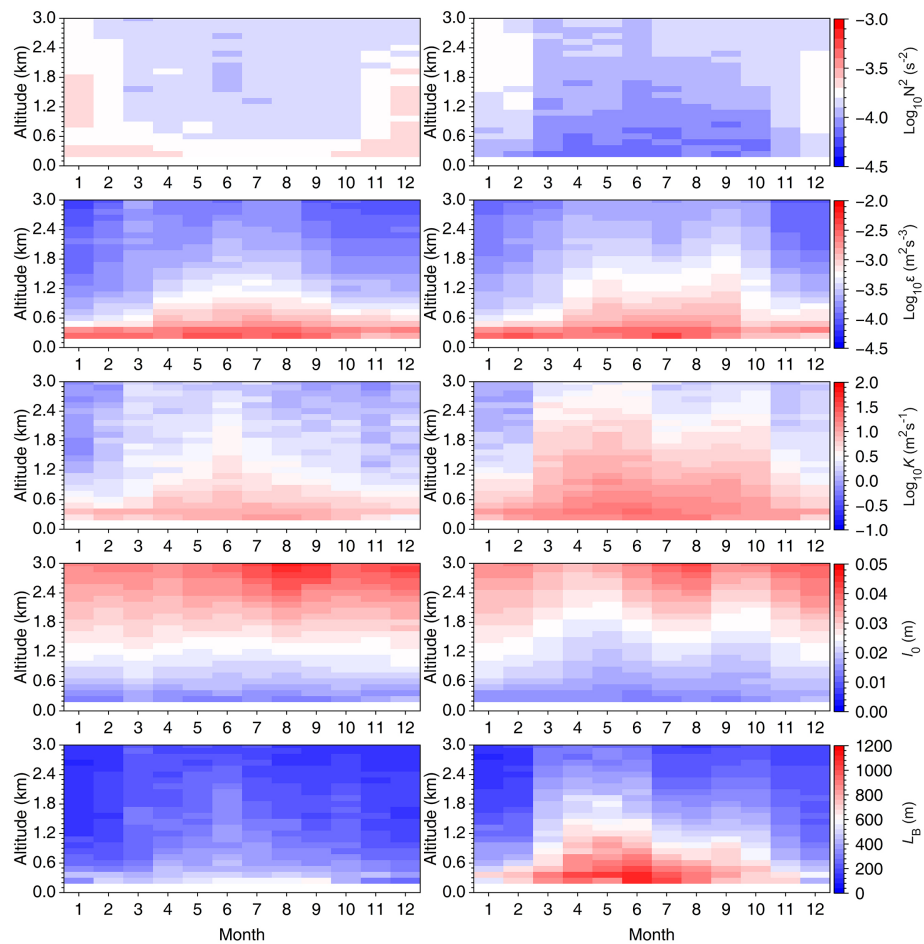
667 **Figure 5.** Vertical profiles of (a) squared Brunt Vaisalä frequency ( $N^2$ ), (b) Richardson  
 668 number ( $Ri$ ), (c) turbulent dissipation rate ( $\epsilon$ ), (d) vertical eddy diffusivity ( $K$ ), (e) inner  
 669 scale ( $l_0$ ) and (f) buoyancy length scale ( $L_B$ ) in the 0.12 to 3.0 km altitude range AGL  
 670 at 00 UTC (blue) and 12 UTC (red) for 2023, and the slope values of turbulence-related  
 671 parameters with altitude are also given in each panel where red and blue values  
 672 represent 00 UTC and 12UTC, respectively.



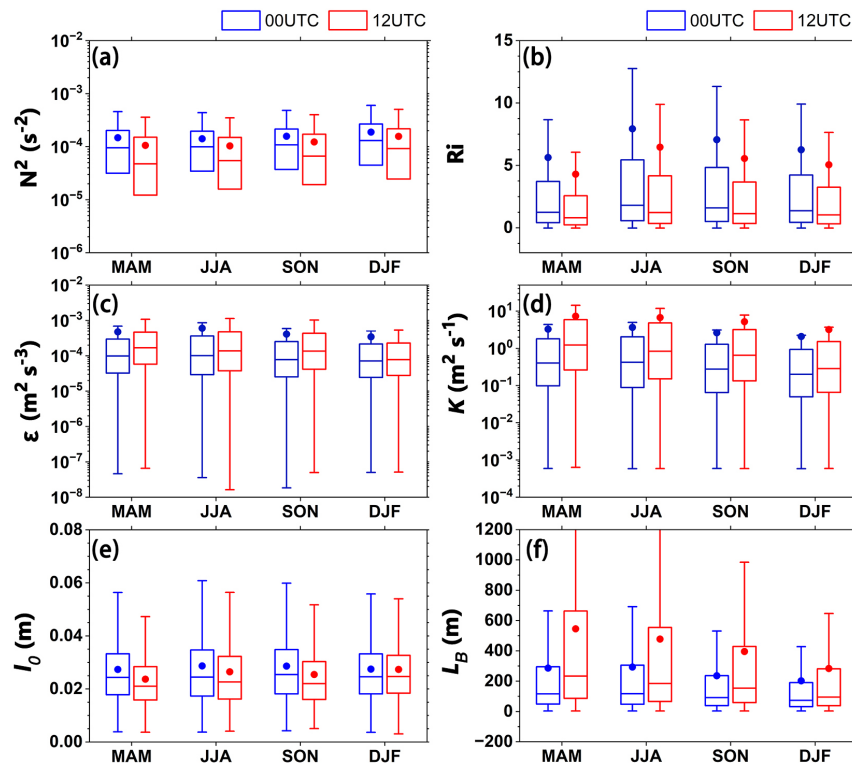
673  
 674 **Figure 6.** The probability density functions (PDF) of (a) squared Brunt Vaisälä  
 675 frequency ( $N^2$ ), (b) Richardson number ( $Ri$ ), (c) turbulent dissipation rate ( $\epsilon$ ), (d)  
 676 vertical eddy diffusivity ( $K$ ), (e) inner scale ( $l_0$ ) and (f) buoyancy length scale ( $L_B$ ) in  
 677 the 0.12 to 3.0 km altitude range AGL at 00 UTC (blue) and 12 UTC (red) for 2023,  
 678 respectively.



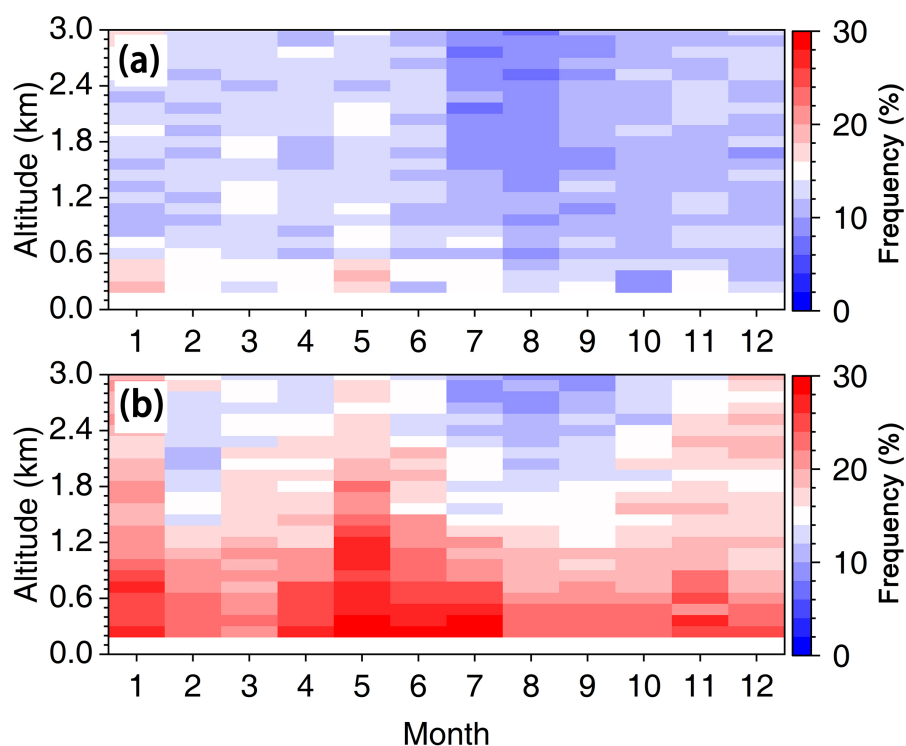
679  
 680 **Figure 7.** The correlation coefficients between turbulence-related parameters at (a) 00  
 681 UTC, (b) 12 UTC, respectively



682  
 683 **Figure 8.** Monthly variation of (a) squared Brunt Vaisala frequency ( $N^2$ ), (b)  
 684 Richardson number ( $Ri$ ), (c) turbulent dissipation rate ( $\epsilon$ ), (d) vertical eddy diffusivity  
 685 ( $K$ ), (e) inner scale ( $l_0$ ) and (f) buoyancy length scale ( $L_B$ ) in the 0.12 to 3.0 km altitude  
 686 range AGL at 00 UTC (left) and 12 UTC (right) for 2023, respectively.



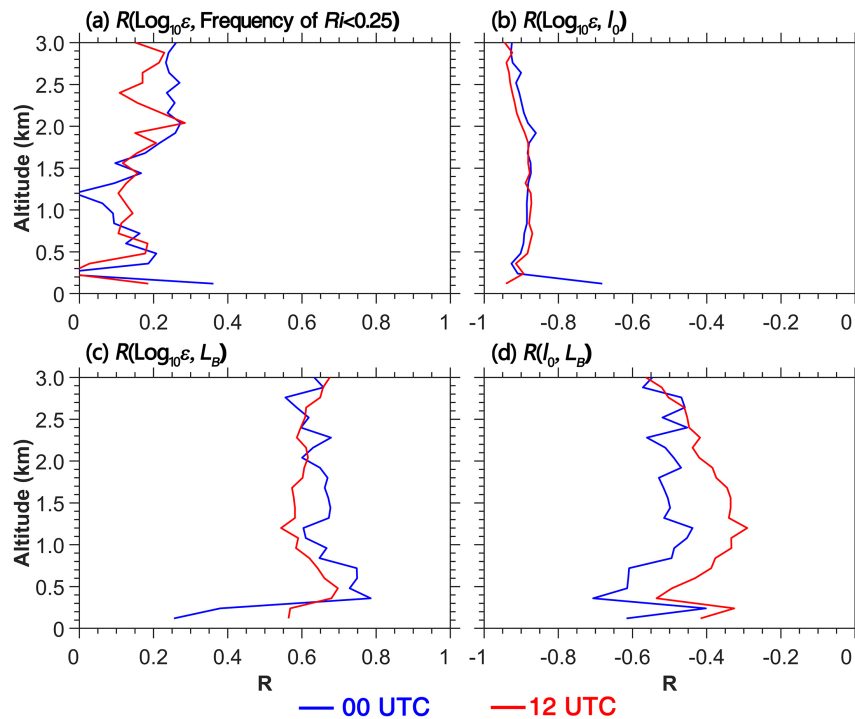
687  
 688 **Figure 9.** Box plot of seasonal (a) squared Brunt Vaisälä frequency ( $N^2$ ), (b)  
 689 Richardson number ( $Ri$ ), (c) turbulent dissipation rate ( $\epsilon$ ), (d) vertical eddy diffusivity  
 690 ( $K$ ), (e) inner scale ( $l_0$ ) and (f) buoyancy length scale ( $L_B$ ) in the 0-3 km height range  
 691 at 00 UTC (light blue) and 12 UTC (light red) for 2023, respectively. Note that the  
 692 median is shown as a line, the mean value is displayed as a circle, whereas the outer  
 693 boundaries of the boxes represent the 25<sup>th</sup> and 75<sup>th</sup> percentiles, and the lines represent  
 694 the interquartile range (IQR). Seasonal divisions are MAM (March-May), JJA (June-  
 695 August), SON (September-November), DJF (December-February), respectively.



696  
 697 **Figure 10.** Monthly variation of occurrence frequency of  $Ri < 0.25$  as a function of  
 698 altitude, spanning from 0.12 to 3.0 km AGL at 00 UTC (a) and 12 UTC (b) for the year  
 699 of 2023, respectively.

700

701



702  
 703 **Figure 11.** Profiles of correlation coefficient ( $R$ ) between (a) turbulent dissipation rate  
 704 ( $\text{Log}_{10}\varepsilon$ ) and the frequency of  $Ri < 0.25$  at 00 UTC (blue) and 12 UTC (red). (b) Same  
 705 as (a) but for the correlations of  $\text{Log}_{10}\varepsilon$  with inner scale ( $l_0$ ). (c) Same as (a) but for the  
 706 correlation of  $\text{Log}_{10}\varepsilon$  with buoyancy length scale ( $L_B$ ). (d) Correlations for  $l_0$  and  $L_B$   
 707 in the inertial subrange, respectively.  
 708